Distributed Angle-Only Relative Orbit Determination in Satellite Networks

Giovanni Romagnoli
Department of Information Engineering
University of Pisa
Pisa 56122, Italy
giovanni.romagnoli@phd.unipi.it

Giordana Bucchioni
Department of Information Engineering
University of Pisa
Pisa 56122, Italy
giordana.bucchioni@unipi.it

Giusy Falcone
Aerospace Engineering
University of Michigan
Ann Arbor, Michigan 48109-2140
falconeg@umich.edu

***Abstract*—**This paper presents a distributed framework for angle-only relative orbit determination in satellite networks, motivated by the increasing need for autonomous and scalable navigation in congested orbital environments. Angles-only approaches are getting a lot of attention because they rely on passive optical sensors, which are lightweight, low-power, and already available on most spacecraft. However, single-observer configurations are strongly limited by poor observability, leading to fragile and inaccurate estimates. To overcome these challenges, we introduce a complete pipeline that integrates three key components: (1) a geometric initialization algorithm that estimates the initial target state from synchronized line-of-sight measurements of multiple observers; (2) an analytical covariance derivation that quantifies the accuracy of the initial estimation, independently of orbital dynamics; and (3) a distributed extended Kalman filter (DEKF) based on information consensus, that fuses measurements across the network to provide continuous tracking of the target spacecraft. Numerical simulations in a realistic low Earth orbit scenario demonstrate that the proposed method achieves estimation performance close to a centralized EKF, while maintaining full distribution and robustness to network topology. The DEKF ensures consensus among observers and limits position errors to a few meters and velocity errors below 10^{-4} km/s, significantly outperforming independent filters. These results prove that consensus-based distributed angle-only navigation can provide accurate and scalable orbit determination capabilities, paving the way for future multi-satellite missions and space-based surveillance architectures.

TABLE OF CONTENTS

1. INTRODUCTION 1
2. INITIAL ORBIT DETERMINATION METHOD 2
3. COVARIANCE ESTIMATION 3
4. DISTRIBUTED FILTERING 5
5. SIMULATION SCENARIO 7
6. NUMERICAL RESULTS AND ANALYSIS 7
7. CONCLUSIONS AND FUTURE WORK 9
ACKNOWLEDGEMENTS 10
REFERENCES 10
BIOGRAPHY 11

979-8-3315-7360-7/26/$31.00 ©2026 IEEE

1. INTRODUCTION

The rapid expansion of human activity in orbit has led to increasingly congested orbital regimes, raising the risk of collisions and making *Space Situational Awareness* (SSA) a critical priority for both civil and defense missions [1]. Traditional SSA architectures rely heavily on ground-based radar and optical monitoring systems. While mature and effective for Earth-orbiting objects, these systems suffer from inherent limitations: restricted visibility due to Earth's rotation and atmosphere, long communication delays for cislunar or deep-space regimes, and scalability challenges in monitoring a rapidly growing population of *resident space objects* (RSOs). To overcome these barriers, there is a growing consensus on the need for *space-based SSA*, where orbital observers provide continuous coverage unconstrained by the Earth's atmosphere [2].

A cornerstone of space-based observation and multi-satellite missions is the ability to achieve autonomous *Relative Orbit Determination* (ROD), namely the estimation of the relative state of nearby RSOs or cooperating spacecraft. Among the available sensing modalities, *angles-only* techniques have emerged as particularly attractive [3]. In this case, the only measurements available are *line-of-sight* (LOS) directions to the observed object, without direct range information. Such measurements are naturally provided by vision-based sensors, including star trackers and navigation cameras, which are already available on most modern spacecraft. These sensors are passive, lightweight, and low-power, while offering high accuracy and wide dynamic range [4]. This makes angles-only ROD especially suitable for distributed and resource-constrained missions.

Despite these advantages, angles-only ROD with a single observer is fundamentally limited by observability: under standard linearized relative dynamics (e.g., Clohessy–Wiltshire equations), the relative range cannot be estimated from bearing directions alone [5]. Several strategies have been proposed to overcome this limitation, including the use of maneuvers to excite the dynamics [5], stereoscopic or displaced cameras to induce parallax [6], or the adoption of richer dynamical models that increase the diversity of angular measurements [7], [8], [9], [10]. However, these solutions remain only partially effective in practice: they often require additional hardware, consume propellant, or depend on extended observation windows.

The feasibility of single-observer angles-only navigation has

nonetheless been demonstrated in orbit. The *ARGON* experiment (DLR, 2012) validated autonomous navigation between two spacecraft relying solely on camera-based angle measurements [11], and the subsequent *AVANTI* mission (DLR, 2016) showcased angles-only guidance and navigation for autonomous proximity operations with a non-cooperative target [12]. These missions underline both the promise of optical navigation and the intrinsic limitations of single-observer geometries: even when feasible, angles-only ROD in this setting remains fragile and heavily constrained.

For these reasons, a natural and promising route is to exploit cooperation among multiple satellites. By fusing LOS measurements from different observation points, geometric ambiguities can be resolved without maneuvers or active sensors. Beyond the geometric benefits, multi-agent architectures align with a broader trend in space exploration: distributed systems and spacecraft swarms are increasingly considered for applications in Earth orbit (e.g., GRACE [13], TanDEM-X [14], MMS [15]) and beyond (e.g., ANS [16]), offering robustness, scalability, and novel capabilities unattainable with monolithic spacecraft.

Within this context, the literature has advanced along several complementary directions. Early work established the observability conditions for multi-observer configurations, showing that geometric diversity can restore the information lost in single-observer scenarios [17]. A graph-theoretic perspective linking target observability to network topology was later introduced, leading to distributed orbit determination methods exploiting this structure [18]. On the estimation side, consensus-based distributed Kalman filters have been shown to approach centralized performance while preserving scalability and robustness in optical tracking networks [19]. A comprehensive framework for cooperative self-navigation and distributed multi-target tracking using only angular measurements was presented in [20], while a geometric initialization method reconstructing the target state from LOS-derived planes and their derivatives was proposed in [21].

Building on these contributions, this work proposes a new approach to distributed angles-only ROD that integrates the main building blocks into a unified framework. A geometric initialization method was extended with a novel analytical procedure to estimate the associated covariance matrix directly from sensor characteristics and other known quantities[21]. This derivation is dynamics-free, relying solely on measurement geometry, and thus remains valid in any orbital regime. The resulting state and covariance estimates are then used to initialize a distributed extended Kalman filter (DEKF) based on consensus on the innovation [22]. While the consensus strategy itself is independent of dynamics, the prediction model can be adapted to the regime of interest, ensuring flexibility across diverse mission scenarios.

The proposed pipeline combines geometric initialization, covariance construction, and distributed filtering into a complete and versatile framework for autonomous angles-only orbit determination in satellite networks. It provides a consistent, analytically grounded, and fully distributed solution that leverages the geometric diversity of multiple observers and is applicable across a broad range of dynamical environments.

2. Initial Orbit Determination Method

The proposed *Initial Orbit Determination* (IOD) method builds upon the geometric approach described in [21], where the state of a target object is reconstructed from simultaneous line-of-sight (LOS) measurements acquired by multiple observer satellites. This section recalls the main steps of the method and introduces the main ingredients of the proposed framework.

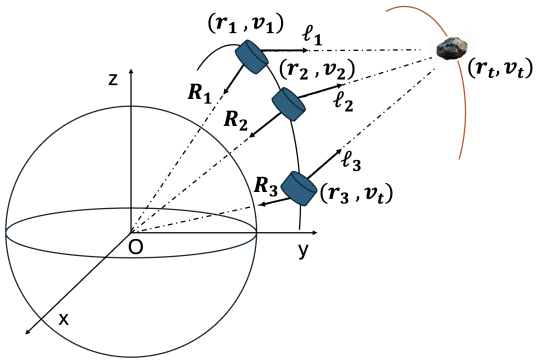

Figure 1. Reference scenario and geometry: observers at $(\boldsymbol{r}_i, \boldsymbol{v}_i)$ measure LOS $\boldsymbol{\ell}_i$ towards the target $(\boldsymbol{r}_t, \boldsymbol{v}_t)$. The unit vectors $\boldsymbol{R}_i = -\boldsymbol{r}_i/\|\boldsymbol{r}_i\|$ define the planes used to define the linear constraints.

Assumptions

Two working assumptions are adopted in this formulation:

- **Assumption 1 (Known observer states).** Each agent i is assumed to know its own inertial position $\boldsymbol{r}_i \in \mathbb{R}^3$ and velocity $\boldsymbol{v}_i \in \mathbb{R}^3$ at the measurement epoch. This is consistent with the focus of the present work, which is on the *relative orbit determination* (ROD) of the target with respect to the observer network. In practice, this assumption can be relaxed: observer states can be supplied from ground-based orbit determination or maintained onboard through cooperative autonomous navigation algorithms, as demonstrated for example in [17].
- **Assumption 2 (Synchronous measurements).** LOS measurements are assumed to be synchronized across the observing agents, i.e.,

$$t_k^{(1)} = t_k^{(2)} = \cdots = t_k^{(N)} = t_k,$$

so that all constraints refer to the same epoch. This greatly simplifies the derivation. While precise synchronization may be challenging in heterogeneous or opportunistic systems, it is realistic in purpose-built missions with inter-satellite communication and clock alignment. Moreover, small timing offsets can be absorbed into the measurement noise model if needed.

Geometric formulation

Consider a network of N observing agents at a given epoch. Each agent measures the LOS unit vector $\boldsymbol{\ell}_i \in \mathbb{R}^3$ towards the target:

$$\boldsymbol{\ell}_i = \frac{\boldsymbol{r}_t - \boldsymbol{r}_i}{\|\boldsymbol{r}_t - \boldsymbol{r}_i\|},$$

and the discrete-time LOS rate (by finite differencing)

$$\dot{\boldsymbol{\ell}}_i(t_k) \approx \frac{\boldsymbol{\ell}_i(t_k) - \boldsymbol{\ell}_i(t_{k-1})}{\Delta t}, \qquad \Delta t = t_k - t_{k-1}. \quad (1)$$

Define $\boldsymbol{R}_i = -\boldsymbol{r}_i/\|\boldsymbol{r}_i\| \in \mathbb{R}^3$ and two orthogonal plane normals

$$\boldsymbol{n}_{1,i} = \boldsymbol{\ell}_i \times \boldsymbol{R}_i, \qquad \boldsymbol{n}_{2,i} = \boldsymbol{n}_{1,i} \times \boldsymbol{\ell}_i \quad (\boldsymbol{n}_{1,i}, \boldsymbol{n}_{2,i} \in \mathbb{R}^3).$$

By construction, the target position $\boldsymbol{r}_t \in \mathbb{R}^3$ lies on the two planes through $\boldsymbol{r}_i$ with normals $\boldsymbol{n}_{1,i}$ and $\boldsymbol{n}_{2,i}$, which implies

$$\boldsymbol{A}_i\, \boldsymbol{r}_t = \boldsymbol{b}_i,$$
$$\boldsymbol{A}_i = \begin{bmatrix} \boldsymbol{n}_{1,i}^\top \\ \boldsymbol{n}_{2,i}^\top \end{bmatrix} \in \mathbb{R}^{2\times 3}, \qquad \boldsymbol{b}_i = \begin{bmatrix} \boldsymbol{n}_{1,i}^\top \boldsymbol{r}_i \\ \boldsymbol{n}_{2,i}^\top \boldsymbol{r}_i \end{bmatrix} \in \mathbb{R}^2. \tag{2}$$

By differentiating these relations, two additional constraints coupling $\boldsymbol{r}_t$ and $\boldsymbol{v}_t$ can be obtained:

$$\dot{\boldsymbol{A}}_i\, \boldsymbol{r}_t + \boldsymbol{A}_i\, \boldsymbol{v}_t = \dot{\boldsymbol{b}}_i, \qquad \dot{\boldsymbol{A}}_i \in \mathbb{R}^{2\times 3},\ \dot{\boldsymbol{b}}_i \in \mathbb{R}^2, \tag{3}$$

where $\dot{\boldsymbol{A}}_i, \dot{\boldsymbol{b}}_i$ are functions of $(\boldsymbol{r}_i, \boldsymbol{v}_i)$ and of the measured $\dot{\boldsymbol{\ell}}_i$.

Stacking all agents yields the global linear system

$$\boldsymbol{\mathcal{H}}\, \boldsymbol{x} = \boldsymbol{y}, \qquad \boldsymbol{x} = \begin{bmatrix} \boldsymbol{r}_t \\ \boldsymbol{v}_t \end{bmatrix} \in \mathbb{R}^6, \tag{4}$$

with block structure and sizes

$$\boldsymbol{\mathcal{H}} = \begin{bmatrix} \boldsymbol{A}_1 & \boldsymbol{0}_{2\times 3} \\ \dot{\boldsymbol{A}}_1 & \boldsymbol{A}_1 \\ \vdots & \vdots \\ \boldsymbol{A}_N & \boldsymbol{0}_{2\times 3} \\ \dot{\boldsymbol{A}}_N & \boldsymbol{A}_N \end{bmatrix} \in \mathbb{R}^{(4N)\times 6} \quad \boldsymbol{y} = \begin{bmatrix} \boldsymbol{b}_1 \\ \dot{\boldsymbol{b}}_1 \\ \vdots \\ \boldsymbol{b}_N \\ \dot{\boldsymbol{b}}_N \end{bmatrix} \in \mathbb{R}^{4N} \tag{5}$$

Since the system is generally overdetermined for $N \geq 2$, the initial estimate of the target state is obtained by least squares:

$$\hat{\boldsymbol{x}} = \arg\min_{\boldsymbol{x}} \|\boldsymbol{\mathcal{H}}\boldsymbol{x} - \boldsymbol{y}\|_2^2, \qquad \hat{\boldsymbol{x}} = (\boldsymbol{\mathcal{H}}^\top \boldsymbol{\mathcal{H}})^{-1} \boldsymbol{\mathcal{H}}^\top \boldsymbol{y}. \tag{6}$$

This provides a consistent initialization of both the target position and velocity solely from synchronized angle-only measurements collected by multiple observers.

3. Covariance Estimation

This section analytically derives an estimate on the covariance of the geometric least–squares (LS) initializer presented in Sec. 2. The key idea is that small angular errors in the line-of-sight (LOS) measurements perturb the geometric constraints and their time derivatives. These perturbations propagate to the final LS state estimate. By linearizing this propagation chain, we obtain a closed–form expression for the state covariance that depends only on the sensor accuracy and the geometry of the observer network, not on the target dynamics.

Throughout, we use the skew-symmetric operator: for any vector $\boldsymbol{a} \in \mathbb{R}^3$, $[\boldsymbol{a}]_\times$ denotes the 3×3 matrix such that $[\boldsymbol{a}]_\times \boldsymbol{b} = \boldsymbol{a} \times \boldsymbol{b}$ for any $\boldsymbol{b} \in \mathbb{R}^3$.

Noise Model on LOS and LOS Rate

Each agent i measures a unit line-of-sight (LOS) vector $\boldsymbol{\ell}_i \in \mathbb{R}^3$ and its rate of change $\dot{\boldsymbol{\ell}}_i \in \mathbb{R}^3$, obtained by finite differencing (see Eq. (1)).

- **Assumption 3 (LOS noise model).** We assume that LOS measurement errors can be represented as small random angular perturbations of the true direction $\boldsymbol{\ell}_i^{\text{true}}$. Specifically:
  - We assume the measurement error is purely angular, meaning the error vector is always orthogonal to the true LOS direction. This reflects the physics of optical sensors, which produce errors in pointing direction, not in the vector's magnitude (which is fixed at unity).
  - We assume the error is isotropic (i.e., has no preferred direction) in the plane perpendicular to the LOS.
  - We assume the magnitude of the angular error follows a zero-mean Gaussian distribution. This is a standard modeling choice that is both physically plausible and mathematically convenient for analysis and filter design.

  To formalize these assumptions, the noisy LOS is modeled as

$$\boldsymbol{\ell}_i = \exp([\theta_i \boldsymbol{u}_i]_\times)\, \boldsymbol{\ell}_i^{\text{true}}, \tag{7}$$

where $\boldsymbol{u}_i \in \mathbb{R}^3$ is a unit vector drawn uniformly at random from the plane orthogonal to $\boldsymbol{\ell}_i^{\text{true}}$, and $\theta_i \sim \mathcal{N}(0, \sigma_\theta^2)$ is a small random angle. This representation corresponds to the standard axis–angle parametrization of rotations, with $\boldsymbol{u}_i$ the rotation axis and θ_i the rotation angle. To first order in θ_i, the perturbation $\delta\boldsymbol{\ell}_i = \boldsymbol{\ell}_i - \boldsymbol{\ell}_i^{\text{true}}$ is

$$\delta\boldsymbol{\ell}_i \approx \theta_i\, [\boldsymbol{u}_i]_\times\, \boldsymbol{\ell}_i^{\text{true}} \tag{8}$$

which guarantees $\delta\boldsymbol{\ell}_i \perp \boldsymbol{\ell}_i^{\text{true}}$. The resulting covariance is the projector onto the tangent plane scaled by the variance of the angular error:

$$\Sigma_\ell = \mathbb{E}[\delta\boldsymbol{\ell}_i\, \delta\boldsymbol{\ell}_i^\top] = \sigma_\theta^2 \big(\boldsymbol{I}_3 - \boldsymbol{\ell}_i \boldsymbol{\ell}_i^\top\big), \tag{9}$$

where the measured $\boldsymbol{\ell}_i$ is used in place of the true one.

Finally, the noise affecting the LOS rate $\dot{\boldsymbol{\ell}}_i$ is directly induced by the differencing of consecutive noisy LOS vectors. Consequently, its statistics depend only on the angular error variance σ_θ^2 and on the differencing interval Δt. Assume the measurement errors at t_k and t_{k-1} are independent and have the same covariance Σ_ℓ (that is, the sensors share the same accuracy), the resulting error covariances for the LOS rate and the cross-covariance are as follows:

$$\begin{aligned} \Sigma_{\dot\ell} &= \frac{2}{\Delta t^2}\, \Sigma_\ell = \frac{2\sigma_\theta^2}{\Delta t^2} \big(\boldsymbol{I}_3 - \boldsymbol{\ell}_i \boldsymbol{\ell}_i^\top\big), \\ \Sigma_{\ell\dot\ell} &= \mathbb{E}\big[\delta\boldsymbol{\ell}_i(t_k)\, \delta\dot{\boldsymbol{\ell}}_i(t_k)^\top\big] = \frac{1}{\Delta t}\, \Sigma_\ell \\ &= \frac{\sigma_\theta^2}{\Delta t} \big(\boldsymbol{I}_3 - \boldsymbol{\ell}_i \boldsymbol{\ell}_i^\top\big) \end{aligned} \tag{10}$$

The joint noise covariance matrix for agent measurements i is therefore the block matrix

$$\boldsymbol{\Sigma}_i = \begin{bmatrix} \Sigma_\ell & \Sigma_{\ell\dot\ell} \\ \Sigma_{\ell\dot\ell}^\top & \Sigma_{\dot\ell} \end{bmatrix} \in \mathbb{R}^{6\times 6}. \tag{11}$$

Linearization of the LS Solution

We recall from eq. (6) that the LS solution is

$$\hat{\boldsymbol{x}} = (\boldsymbol{\mathcal{H}}^\top \boldsymbol{\mathcal{H}})^{-1} \boldsymbol{\mathcal{H}}^\top \boldsymbol{y}.$$

Noise in the LOS measurements induces perturbations also in the system matrix and vector:

$$(\boldsymbol{\mathcal{H}}, \boldsymbol{y}) \mapsto (\boldsymbol{\mathcal{H}} + \delta\boldsymbol{\mathcal{H}},\ \boldsymbol{y} + \delta\boldsymbol{y}).$$

Let $\boldsymbol{M} \doteq \boldsymbol{\mathcal{H}}^\top \boldsymbol{\mathcal{H}}$. The perturbed state estimate is

$$\begin{aligned}\hat{\boldsymbol{x}}^+ = \big((\boldsymbol{\mathcal{H}} + \delta\boldsymbol{\mathcal{H}})^\top (\boldsymbol{\mathcal{H}} + \delta\boldsymbol{\mathcal{H}})\big)^{-1} \\ \times (\boldsymbol{\mathcal{H}} + \delta\boldsymbol{\mathcal{H}})^\top (\boldsymbol{y} + \delta\boldsymbol{y}).\end{aligned} \tag{12}$$

To find the first-order perturbation in the state, $\delta\boldsymbol{x} \doteq \hat{\boldsymbol{x}}^+ - \hat{\boldsymbol{x}}$, we linearize this expression. Using the identity

$$(\boldsymbol{M} + \delta\boldsymbol{M})^{-1} \approx \boldsymbol{M}^{-1} - \boldsymbol{M}^{-1}\delta\boldsymbol{M}\,\boldsymbol{M}^{-1},$$

with $\delta\boldsymbol{M} \doteq \delta\boldsymbol{\mathcal{H}}^\top\boldsymbol{\mathcal{H}} + \boldsymbol{\mathcal{H}}^\top\delta\boldsymbol{\mathcal{H}}$ and neglecting all second-order terms (products of perturbations), we obtain:

$$\begin{aligned}\delta\boldsymbol{x} \;\approx\; & \boldsymbol{M}^{-1}\boldsymbol{\mathcal{H}}^\top\delta\boldsymbol{y} + \boldsymbol{M}^{-1}\delta\boldsymbol{\mathcal{H}}^\top\boldsymbol{y} \\ & - \boldsymbol{M}^{-1}\big(\delta\boldsymbol{\mathcal{H}}^\top\boldsymbol{\mathcal{H}} + \boldsymbol{\mathcal{H}}^\top\delta\boldsymbol{\mathcal{H}}\big)\hat{\boldsymbol{x}}.\end{aligned} \tag{13}$$

Assuming that the linearization is performed around the true state $\boldsymbol{x}$, for which the residuals are zero ($\boldsymbol{y} = \boldsymbol{\mathcal{H}}\boldsymbol{x}$), and noting that $\hat{\boldsymbol{x}} = \boldsymbol{x}$ in this noise–free reference point (i.e., the LS estimate coincides with the true state when evaluated with exact measurements), the expression simplifies significantly:

$$\delta\boldsymbol{x} \approx \boldsymbol{M}^{-1}\boldsymbol{\mathcal{H}}^\top\big(\delta\boldsymbol{y} - \delta\boldsymbol{\mathcal{H}}\,\boldsymbol{x}\big). \tag{14}$$

This relation relates the state error $\delta\boldsymbol{x}$ to the perturbation of the residual, which we define as

$$\delta\boldsymbol{e} \doteq \delta\boldsymbol{y} - \delta\boldsymbol{\mathcal{H}}\,\boldsymbol{x}.$$

The vector $\delta\boldsymbol{e} \in \mathbb{R}^{4N}$ stacks the residual perturbations from all N agents, $\delta\boldsymbol{e} = [\delta\boldsymbol{e}_1^\top, \ldots, \delta\boldsymbol{e}_N^\top]^\top$.

The relationship can be written compactly as

$$\begin{aligned}\delta\boldsymbol{x} &= \boldsymbol{K}\,\delta\boldsymbol{e}, \\ \text{with } \boldsymbol{K} &\doteq (\boldsymbol{\mathcal{H}}^\top\boldsymbol{\mathcal{H}})^{-1}\boldsymbol{\mathcal{H}}^\top \in \mathbb{R}^{6\times 4N}.\end{aligned} \tag{15}$$

From this, the covariance of the LS solution follows directly as

$$\mathrm{Cov}(\hat{\boldsymbol{x}}) = \boldsymbol{K}\,\mathrm{Cov}(\delta\boldsymbol{e})\,\boldsymbol{K}^\top. \tag{16}$$

From Measurement Noise to Residual Perturbation

For each agent i, the residual vector is defined as

$$\boldsymbol{e}_i = \boldsymbol{y}_i - \boldsymbol{\mathcal{H}}_i\boldsymbol{x},$$

where the full system $(\boldsymbol{\mathcal{H}}, \boldsymbol{y})$ was introduced in eq. (4) - (5). For clarity, we now isolate the contribution of a single agent i as

$$\boldsymbol{\mathcal{H}}_i = \begin{bmatrix}\boldsymbol{A}_i & \boldsymbol{0} \\ \dot{\boldsymbol{A}}_i & \boldsymbol{A}_i\end{bmatrix} \in \mathbb{R}^{4\times 6}, \qquad \boldsymbol{y}_i = \begin{bmatrix}\boldsymbol{b}_i \\ \dot{\boldsymbol{b}}_i\end{bmatrix} \in \mathbb{R}^4.$$

Expanding this expression leads to

$$\boldsymbol{e}_i = \begin{bmatrix}\boldsymbol{b}_i - \boldsymbol{A}_i\boldsymbol{r}_t \\ \dot{\boldsymbol{b}}_i - \dot{\boldsymbol{A}}_i\boldsymbol{r}_t - \boldsymbol{A}_i\boldsymbol{v}_t\end{bmatrix}.$$

Recalling that the rows of $\boldsymbol{A}_i$ are $\boldsymbol{n}_{1,i}^\top$ and $\boldsymbol{n}_{2,i}^\top$ (see eq. (2)), and defining the true relative position and velocity as

$$\boldsymbol{\rho}_i \doteq \boldsymbol{r}_i - \boldsymbol{r}_t, \qquad \boldsymbol{\eta}_i \doteq \boldsymbol{v}_i - \boldsymbol{v}_t,$$

the four scalar components of the residual vector can be written as

$$e_{1,i} = \boldsymbol{n}_{1,i}^\top\boldsymbol{\rho}_i, \tag{17}$$

$$e_{2,i} = \boldsymbol{n}_{2,i}^\top\boldsymbol{\rho}_i, \tag{18}$$

$$e_{3,i} = \dot{\boldsymbol{n}}_{1,i}^\top\boldsymbol{\rho}_i + \boldsymbol{n}_{1,i}^\top\boldsymbol{\eta}_i, \tag{19}$$

$$e_{4,i} = \dot{\boldsymbol{n}}_{2,i}^\top\boldsymbol{\rho}_i + \boldsymbol{n}_{2,i}^\top\boldsymbol{\eta}_i. \tag{20}$$

The perturbation $\delta\boldsymbol{e}_i$ is then the vector of first-order differentials

$$\delta\boldsymbol{e}_i = \begin{bmatrix}\delta e_{1,i} \\ \delta e_{2,i} \\ \delta e_{3,i} \\ \delta e_{4,i}\end{bmatrix},$$

whose explicit dependence on the LOS perturbations $\delta\boldsymbol{\ell}_i$ and $\delta\dot{\boldsymbol{\ell}}_i$ will be derived in the next step.

To compute these differentials, we first need to derive the variations of the normal vectors $\boldsymbol{n}_{1,i}, \boldsymbol{n}_{2,i}$ and their time derivatives with respect to the measurement noises $\delta\boldsymbol{\ell}_i$ and $\delta\dot{\boldsymbol{\ell}}_i$. The observer states $(\boldsymbol{r}_i, \boldsymbol{v}_i)$ and thus $\boldsymbol{R}_i = -\boldsymbol{r}_i/\|\boldsymbol{r}_i\|$ are known, so their variations vanish. Applying the product rule for differentiation we get:

$$\delta\boldsymbol{n}_{1,i} = \delta\boldsymbol{\ell}_i \times \boldsymbol{R}_i = -[\boldsymbol{R}_i]_\times\,\delta\boldsymbol{\ell}_i, \tag{21}$$

$$\begin{aligned}\delta\boldsymbol{n}_{2,i} &= \delta\boldsymbol{n}_{1,i} \times \boldsymbol{\ell}_i + \boldsymbol{n}_{1,i} \times \delta\boldsymbol{\ell}_i \\ &= \big(-[\boldsymbol{\ell}_i]_\times[\boldsymbol{R}_i]_\times + [\boldsymbol{n}_{1,i}]_\times\big)\delta\boldsymbol{\ell}_i,\end{aligned} \tag{22}$$

$$\begin{aligned}\delta\dot{\boldsymbol{n}}_{1,i} &= \delta\dot{\boldsymbol{\ell}}_i \times \boldsymbol{R}_i + \delta\boldsymbol{\ell}_i \times \dot{\boldsymbol{R}}_i \\ &= -[\boldsymbol{R}_i]_\times\,\delta\dot{\boldsymbol{\ell}}_i - [\dot{\boldsymbol{R}}_i]_\times\,\delta\boldsymbol{\ell}_i,\end{aligned} \tag{23}$$

$$\begin{aligned}\delta\dot{\boldsymbol{n}}_{2,i} &= \delta\dot{\boldsymbol{n}}_{1,i} \times \boldsymbol{\ell}_i + \dot{\boldsymbol{n}}_{1,i} \times \delta\boldsymbol{\ell}_i + \delta\boldsymbol{n}_{1,i} \times \dot{\boldsymbol{\ell}}_i + \boldsymbol{n}_{1,i} \times \delta\dot{\boldsymbol{\ell}}_i \\ &= \big([\boldsymbol{\ell}_i]_\times[\boldsymbol{R}_i]_\times + [\boldsymbol{n}_{1,i}]_\times\big)\delta\dot{\boldsymbol{\ell}}_i \\ &\quad + \big([\boldsymbol{\ell}_i]_\times[\dot{\boldsymbol{R}}_i]_\times + [\dot{\boldsymbol{n}}_{1,i}]_\times + [\dot{\boldsymbol{\ell}}_i]_\times[\boldsymbol{R}_i]_\times\big)\delta\boldsymbol{\ell}_i.\end{aligned} \tag{24}$$

Here, the time derivative of the radial unit vector is

$$\dot{\boldsymbol{R}}_i = -\frac{1}{\|\boldsymbol{r}_i\|}\big(\boldsymbol{I}_3 - \boldsymbol{R}_i\boldsymbol{R}_i^\top\big)\boldsymbol{v}_i.$$

Substituting equations (21)-(24) into the expressions for the residuals, we find the linear relationship between the measurement noise and the residual perturbation for agent i:

$$\delta e_{1,i} = \delta\boldsymbol{n}_{1,i}^\top\boldsymbol{\rho}_i, \tag{25}$$

$$\delta e_{2,i} = \delta\boldsymbol{n}_{2,i}^\top\boldsymbol{\rho}_i, \tag{26}$$

$$\delta e_{3,i} = \delta\dot{\boldsymbol{n}}_{1,i}^\top\boldsymbol{\rho}_i + \delta\boldsymbol{n}_{1,i}^\top\boldsymbol{\eta}_i, \tag{27}$$

$$\delta e_{4,i} = \delta\dot{\boldsymbol{n}}_{2,i}^\top\boldsymbol{\rho}_i + \delta\boldsymbol{n}_{2,i}^\top\boldsymbol{\eta}_i. \tag{28}$$

This can be expressed in matrix form as:

$$\delta\boldsymbol{e}_i = \boldsymbol{J}_i\begin{bmatrix}\delta\boldsymbol{\ell}_i \\ \delta\dot{\boldsymbol{\ell}}_i\end{bmatrix}, \qquad \boldsymbol{J}_i \in \mathbb{R}^{4\times 6},$$

where the Jacobian matrix $\boldsymbol{J}_i$ is shown in full in eq. (29).

$$\boldsymbol{J}_i = \begin{bmatrix} -\boldsymbol{\rho}_i^\top [\boldsymbol{R}_i]_\times & \mathbf{0}^\top \\ \boldsymbol{\rho}_i^\top \big(-[\boldsymbol{\ell}_i]_\times [\boldsymbol{R}_i]_\times + [\boldsymbol{n}_{1,i}]_\times \big) & \mathbf{0}^\top \\ -\boldsymbol{\rho}_i^\top [\dot{\boldsymbol{R}}_i]_\times - \boldsymbol{\eta}_i^\top [\boldsymbol{R}_i]_\times & -\boldsymbol{\rho}_i^\top [\boldsymbol{R}_i]_\times \\ \boldsymbol{\rho}_i^\top \big([\boldsymbol{\ell}_i]_\times [\dot{\boldsymbol{R}}_i]_\times + [\dot{\boldsymbol{n}}_{1,i}]_\times + [\dot{\boldsymbol{\ell}}_i]_\times [\boldsymbol{R}_i]_\times \big) + \boldsymbol{\eta}_i^\top \big(-[\boldsymbol{\ell}_i]_\times [\boldsymbol{R}_i]_\times + [\boldsymbol{n}_{1,i}]_\times \big) & \boldsymbol{\rho}_i^\top \big([\boldsymbol{\ell}_i]_\times [\boldsymbol{R}_i]_\times + [\boldsymbol{n}_{1,i}]_\times \big) \end{bmatrix}. \tag{29}$$

Final State Covariance

Using the linear map defined by $\boldsymbol{J}_i$, the covariance of the residual perturbation for a single agent is

$$\mathrm{Cov}(\delta \boldsymbol{e}_i) = \boldsymbol{J}_i \boldsymbol{\Sigma}_i \boldsymbol{J}_i^\top \in \mathbb{R}^{4\times 4}, \tag{30}$$

where $\boldsymbol{\Sigma}_i$ is the joint measurement noise covariance from (11). Since we assume measurement errors are uncorrelated between agents, the covariance matrix of the stacked residual perturbation vector $\delta \boldsymbol{e}$ is block-diagonal:

$$\mathrm{Cov}(\delta \boldsymbol{e}) = \mathrm{diag}\big(\mathrm{Cov}(\delta \boldsymbol{e}_1), \ldots, \mathrm{Cov}(\delta \boldsymbol{e}_N)\big), \qquad \mathrm{Cov}(\delta \boldsymbol{e}) \in \mathbb{R}^{4N\times 4N} \tag{31}$$

Finally, substituting this into (16) gives the desired covariance of the LS state estimate:

$$\mathrm{Cov}(\hat{\boldsymbol{x}}) = \boldsymbol{K}\, \mathrm{diag}\big(\boldsymbol{J}_1 \boldsymbol{\Sigma}_1 \boldsymbol{J}_1^\top, \ldots, \boldsymbol{J}_N \boldsymbol{\Sigma}_N \boldsymbol{J}_N^\top\big)\, \boldsymbol{K}^\top, \tag{32}$$

where $\mathrm{Cov}(\hat{\boldsymbol{x}}) \in \mathbb{R}^{6\times 6}$ and $\boldsymbol{K} \in \mathbb{R}^{6\times 4N}$ is defined in (15). This expression provides the complete first-order uncertainty of the initializer.

4. Distributed Filtering

Once the target state is initialized with the geometric procedure and its covariance is derived (Secs. 2–3), the next step is to transition to sequential tracking. This requires a recursive filter that can incorporate new measurements over time and maintain accuracy in a distributed fashion.

As a benchmark, a *centralized Extended Kalman Filter* (EKF) would combine the measurements from all the agents at a single fusion node, obtaining an optimal estimate. However, such a setup is not ideal in satellite networks, where communication bandwidth is limited and robustness is critical. Instead, we adopt a *Distributed Extended Kalman Filter* (DEKF) based on *consensus on information* [22]. The central idea is that each agent computes additive information terms (innovation and information matrix) from its local measurements, then reaches agreement with neighbors through a lightweight consensus routine. This guarantees statistical consistency, exploits the independence of LOS measurements, and avoids the need for a central fusion node, making the system robust to single point failure. It is important to note that, in this architecture, agents never exchange their state estimates or covariances. Only compact information derived from the local measurements is shared among neighbors during consensus, while each spacecraft maintains and updates its own filter locally.

Process and measurement models

The global state is defined as

$$\boldsymbol{x}_k = \begin{bmatrix} \boldsymbol{r}_t(k) \\ \boldsymbol{v}_t(k) \end{bmatrix} \in \mathbb{R}^6,$$

where $\boldsymbol{r}_t$ and $\boldsymbol{v}_t$ are the inertial position and velocity of the target at time k.

The nonlinear process model is expressed in discrete time as

$$\boldsymbol{x}_{k+1} = f(\boldsymbol{x}_k) + \boldsymbol{w}_k, \qquad \boldsymbol{w}_k \sim \mathcal{N}(\mathbf{0}, \boldsymbol{Q}), \tag{33}$$

where dt is the sampling interval and $\boldsymbol{Q} \in \mathbb{R}^{6\times 6}$ is the process noise covariance. The state evolution function is

$$f(\boldsymbol{x}) = \boldsymbol{x} + dt \begin{bmatrix} \boldsymbol{v}_t \\ -\mu \dfrac{\boldsymbol{r}_t}{\|\boldsymbol{r}_t\|^3} + \boldsymbol{a}_{J_2}(\boldsymbol{r}_t) \end{bmatrix}, \tag{34}$$

with the J_2 perturbation term

$$\boldsymbol{a}_{J_2}(\boldsymbol{r}_t) = \frac{3J_2\mu R_e^2}{2\|\boldsymbol{r}_t\|^5} \begin{bmatrix} x_t \left(1 - 5\dfrac{z_t^2}{\|\boldsymbol{r}_t\|^2}\right) \\ y_t \left(1 - 5\dfrac{z_t^2}{\|\boldsymbol{r}_t\|^2}\right) \\ z_t \left(3 - 5\dfrac{z_t^2}{\|\boldsymbol{r}_t\|^2}\right) \end{bmatrix}. \tag{35}$$

Here $(x_t\ y_t\ z_t)$ are the components of the target inertial position vector, μ is the gravitational parameter, R_e the Earth's mean equatorial radius, and J_2 the second zonal harmonic coefficient. The measurement available to agent i at time k is the normalized line-of-sight (LOS):

$$\boldsymbol{\ell}_k^i = h^i(\boldsymbol{x}_k) + \boldsymbol{\nu}_k^i, \qquad h^i(\boldsymbol{x}) = \frac{\boldsymbol{r}_t - \boldsymbol{r}_i}{\|\boldsymbol{r}_t - \boldsymbol{r}_i\|}, \tag{36}$$

where $\boldsymbol{\nu}_k^i \sim \mathcal{N}(\mathbf{0}, \boldsymbol{\mathcal{R}}^i)$ is the measurement noise with covariance $\boldsymbol{\mathcal{R}}^i \in \mathbb{R}^{3\times 3}$.

Jacobian matrices

The EKF requires linearization of both dynamics and measurements.

The process Jacobian is

$$\boldsymbol{F}_k = \frac{\partial f}{\partial \boldsymbol{x}} = \begin{bmatrix} \boldsymbol{I}_{3\times 3} & dt\, \boldsymbol{I}_{3\times 3} \\ dt \left(\dfrac{\partial \boldsymbol{a}_{\text{grav}}}{\partial \boldsymbol{r}_t} + \dfrac{\partial \boldsymbol{a}_{J_2}}{\partial \boldsymbol{r}_t} \right) & \boldsymbol{I}_{3\times 3} \end{bmatrix}, \tag{37}$$

where the Keplerian component is

$$\frac{\partial \boldsymbol{a}_{\text{grav}}}{\partial \boldsymbol{r}_t} = -\mu \left(\frac{\boldsymbol{I}}{r_t^3} - 3\, \frac{\boldsymbol{r}_t \boldsymbol{r}_t^\top}{r_t^5} \right), \qquad r_t = \|\boldsymbol{r}_t\|.$$

For the J_2 contribution, let $\boldsymbol{r}_t = (x_t, y_t, z_t)$ and define

$$k = \frac{3J_2\mu R_e^2}{2}.$$

Then

$$\frac{\partial \boldsymbol{a}_{J_2}}{\partial \boldsymbol{r}_t} = \begin{bmatrix} \frac{\partial a_x}{\partial x_t} & \frac{\partial a_x}{\partial y_t} & \frac{\partial a_x}{\partial z_t} \\ \frac{\partial a_y}{\partial x_t} & \frac{\partial a_y}{\partial y_t} & \frac{\partial a_y}{\partial z_t} \\ \frac{\partial a_z}{\partial x_t} & \frac{\partial a_z}{\partial y_t} & \frac{\partial a_z}{\partial z_t} \end{bmatrix},$$

with elements

$$\frac{\partial a_x}{\partial x_t} = k\left(\frac{1}{r_t^5} - \frac{5(x_t^2+z_t^2)}{r_t^7} + \frac{35x_t^2z_t^2}{r_t^9}\right),$$

$$\frac{\partial a_x}{\partial y_t} = k\left(-\frac{5x_ty_t}{r_t^7} + \frac{35x_ty_tz_t^2}{r_t^9}\right),$$

$$\frac{\partial a_x}{\partial z_t} = k\left(-\frac{15x_tz_t}{r_t^7} + \frac{35x_tz_t^3}{r_t^9}\right),$$

$$\frac{\partial a_y}{\partial y_t} = k\left(\frac{1}{r_t^5} - \frac{5(y_t^2+z_t^2)}{r_t^7} + \frac{35y_t^2z_t^2}{r_t^9}\right),$$

$$\frac{\partial a_y}{\partial z_t} = k\left(-\frac{15y_tz_t}{r_t^7} + \frac{35y_tz_t^3}{r_t^9}\right),$$

$$\frac{\partial a_z}{\partial z_t} = k\left(\frac{3}{r_t^5} - \frac{30z_t^2}{r_t^7} + \frac{35z_t^4}{r_t^9}\right).$$

The matrix is symmetric, since it derives from the Hessian of the J_2 gravitational potential. Therefore, the off–diagonal elements satisfy

$$\frac{\partial a_y}{\partial x_t} = \frac{\partial a_x}{\partial y_t}, \qquad \frac{\partial a_z}{\partial x_t} = \frac{\partial a_x}{\partial z_t}, \qquad \frac{\partial a_z}{\partial y_t} = \frac{\partial a_y}{\partial z_t}.$$

For agent i, the measurement Jacobian is obtained through a single linearization around the predicted state:

$$\boldsymbol{H}_k^i = \frac{\partial h^i}{\partial \boldsymbol{x}} = \left[\frac{1}{\|\boldsymbol{\rho}_i\|}\left(\boldsymbol{I} - \frac{\boldsymbol{\rho}_i\boldsymbol{\rho}_i^\top}{\|\boldsymbol{\rho}_i\|^2}\right) \quad \boldsymbol{0}_{3\times 3}\right]. \tag{38}$$

Distributed EKF with information consensus

The DEKF consists in the following steps at each time step k:

1. Prediction. Each agent i propagates its state and covariance:

$$\hat{\boldsymbol{x}}_{k|k-1}^i = f(\hat{\boldsymbol{x}}_{k-1}^i), \tag{39}$$

$$\boldsymbol{P}_{k|k-1}^i = \boldsymbol{F}_{k-1}\boldsymbol{P}_{k-1}^i\boldsymbol{F}_{k-1}^\top + N\,\boldsymbol{Q}, \tag{40}$$

where the scaling by N (number of agents) ensures equivalence with centralized information fusion when consensus converges [22].

2. Information terms computation. Each agent i computes the local additive quantities

$$\boldsymbol{z}_k^i = (\boldsymbol{H}_k^i)^\top(\boldsymbol{\mathcal{R}}^i)^{-1}\,\boldsymbol{\ell}_k^i, \tag{41}$$

$$\bar{\boldsymbol{z}}_k^i = (\boldsymbol{H}_k^i)^\top(\boldsymbol{\mathcal{R}}^i)^{-1}\,h^i(\hat{\boldsymbol{x}}_{k|k-1}^i), \tag{42}$$

$$\boldsymbol{S}_k^i = (\boldsymbol{H}_k^i)^\top(\boldsymbol{\mathcal{R}}^i)^{-1}\,\boldsymbol{H}_k^i. \tag{43}$$

Here $\boldsymbol{z}_k^i, \bar{\boldsymbol{z}}_k^i \in \mathbb{R}^6$ are information-weighted versions of the actual and predicted LOS, while $\boldsymbol{S}_k^i \in \mathbb{R}^{6\times 6}$ is the local information matrix, symmetric and positive semidefinite, quantifying how informative sensor i is about the target state.

3. Consensus. Each agent exchanges the information terms $(\boldsymbol{z}_k^i, \bar{\boldsymbol{z}}_k^i, \boldsymbol{S}_k^i)$ only with its neighbors $\mathcal{N}_i$, where $\mathcal{N}_i$ denotes the set of nodes directly connected to agent i in the communication graph. The exchange is repeated for a fixed number of consensus iterations, during which each node updates its variables as weighted averages with those received from neighbors. The consensus iterations are assumed to be instantaneous with respect to the orbital dynamics, occurring entirely within the sampling interval. This low-pass consensus filter [22] asymptotically leads all agents toward aligned values $(\boldsymbol{z}_k, \bar{\boldsymbol{z}}_k, \boldsymbol{S}_k)$ without requiring global communication or a fusion center.

4. Correction. After a finite number of consensus iterations, each agent i holds its own versions $(\boldsymbol{z}_k^i, \bar{\boldsymbol{z}}_k^i, \boldsymbol{S}_k^i)$, which approximate the global information but are in general not identical across the network. Using these locally available terms, agent i performs the update

$$\boldsymbol{P}_k^i = \left((\boldsymbol{P}_{k|k-1}^i)^{-1} + \boldsymbol{S}_k^i\right)^{-1}, \tag{44}$$

$$\hat{\boldsymbol{x}}_k^i = \hat{\boldsymbol{x}}_{k|k-1}^i + \boldsymbol{P}_k^i(\boldsymbol{z}_k^i - \bar{\boldsymbol{z}}_k^i). \tag{45}$$

Here $\boldsymbol{P}_k^i$ is the corrected covariance and $\hat{\boldsymbol{x}}_k^i$ the corrected state estimate at agent i. Because the information terms $(\boldsymbol{z}_k^i, \bar{\boldsymbol{z}}_k^i, \boldsymbol{S}_k^i)$ are shaped by local measurements but influenced by consensus with neighbors, the correction step reflects both the agent's own observation and the information indirectly received from the rest of the network.

Initialization

At $k = 0$, each agent i performs the IOD process described in Sec. 2 using only the LOS (and LOS-rate from finite differencing) available within its neighborhood $\mathcal{N}_i$. This provides a local state estimate $\hat{\boldsymbol{x}}_0^i$ and an associated covariance $\boldsymbol{P}_0^i = \mathrm{Cov}(\hat{\boldsymbol{x}}_0^i)$, obtained through the procedure described in Sec. 3. Because each agent exploits only partial information, the resulting priors differ across the network.

To initialize the distributed filter consistently, a consensus phase is then performed on both states and covariances. After this alignment step, each agent sets

$$\hat{\boldsymbol{x}}_0^i = \frac{1}{N}\sum_{j=1}^{N}\hat{\boldsymbol{x}}_0^j, \qquad \boldsymbol{P}_0^i = N\,\bar{\boldsymbol{P}}_0,$$

where $\bar{\boldsymbol{P}}_0$ is the consensus average of the local covariance estimates. This guarantees that all agents start the recursive DEKF from a coherent and statistically consistent prior.

Summary

The information-consensus EKF enables each satellite to maintain a local filter while exchanging only compact information terms with neighbors. The method is statistically consistent, fully distributed, and converges to the centralized EKF under ideal consensus, while remaining robust to realistic communication constraints in satellite networks.

For clarity, Algorithm 1 summarizes the proposed pipeline, from geometric initialization to distributed EKF tracking.

Algorithm 1 Distributed Angle-Only Navigation via Geometric IOD and DEKF

Input:

LOS and LOS-rate measurements $\{\boldsymbol{\ell}_i, \dot{\boldsymbol{\ell}}_i\}$,
Observer states $(\boldsymbol{r}_i, \boldsymbol{v}_i)$
Process and measurement noise covariances $(\boldsymbol{Q}, \boldsymbol{\mathcal{R}})$

1. **Geometric IOD**: each agent i computes $(\hat{\boldsymbol{x}}_0^i, \boldsymbol{P}_0^i)$ from its own and neighbors' LOS data.
2. **Consensus Alignment**: agents exchange $(\hat{\boldsymbol{x}}_0^i, \boldsymbol{P}_0^i)$ with neighbors $\mathcal{N}_i$; a short consensus phase aligns priors across the network.
3. **Recursive DEKF**: for each time k

3.1. *Prediction*: propagate $(\hat{\boldsymbol{x}}_{k|k-1}^i, \boldsymbol{P}_{k|k-1}^i)$ with orbital dynamics.
3.2. *Local Information*: compute $(\boldsymbol{z}_k^i, \bar{\boldsymbol{z}}_k^i, \boldsymbol{S}_k^i)$ (see Sec. 4).
3.3. *Consensus*: exchange these terms with $\mathcal{N}_i$ for a fixed number of iterations.
3.4. *Correction*: update $(\hat{\boldsymbol{x}}_{k|k}^i, \boldsymbol{P}_{k|k}^i)$ using the consensus-influenced terms.

Output:

Local estimates $\hat{\boldsymbol{x}}_{k|k}^i$, $\boldsymbol{P}_{k|k}^i$ at each agent.

5. SIMULATION SCENARIO

The numerical simulations are performed in a Low Earth Orbit (LEO) environment. Both the observer constellation and the target are propagated with the `SGP4` model [23], the standard analytical orbit propagator used in conjunction with Two-Line Elements (TLEs). SGP4 accounts for the dominant perturbations acting on near-Earth satellites (e.g., J_2 oblateness, atmospheric drag, luni-solar effects), and provides reliable ground-truth trajectories over limited time spans. All tests have been performed in the `MATLAB` environment, using the reference open-source implementation [24] for orbit propagation.

The observer network consists of three satellites arranged in an in–track formation. All observers share the same orbital elements and differ only in mean anomaly, which creates a stable trailing geometry without the need of active station–keeping. The nominal parameters of the observer constellation are listed in Table 1.

Table 1. Nominal orbital parameters of the observer constellation.

Parameter	Value
Semi-major axis a	6963 km
Eccentricity e	0.0001
Inclination i	85.0°
RAAN Ω	10.0°
Argument of perigee ω	14.0°
Mean anomaly M	288°, 290°, 292°
Propagation model	SGP4

The target is placed on a slightly different orbit and its orbital parameters are listed in Table 2.

The difference in inclination (86.0° vs. 85.0°) and semi–major axis (6949 km vs. 6963 km) guarantees relative drift between target and observers, while the similarity in RAAN and argument of perigee ensures that the target periodically crosses the formation's field of regard. This geometry is representative of a tracking scenario in which a constellation monitors a nearby but not co–orbital object.

Table 2. Nominal orbital parameters of the target.

Parameter	Value
Semi-major axis a	6949 km
Eccentricity e	0.0001
Inclination i	86.0°
RAAN Ω	10.0°
Argument of perigee ω	14.0°
Mean anomaly M	290.0°
Propagation model	SGP4

The communication network among observers is modeled as a line graph, with communication restricted to immediate neighbors:

$$\text{Agent 1} \longleftrightarrow \text{Agent 2} \longleftrightarrow \text{Agent 3}$$

This non–fully connected topology reflects realistic constraints and highlights the role of the consensus–based filtering algorithm, which must propagate information across multiple hops. At each filtering step, 25 consensus iterations are performed.

Every agent obtains LOS measurements every $\Delta t = 0.1$ min (6 s). Only epochs in which the target lies within 500 km of the formation are processed, reflecting the limited optical sensors' field of view. While operational encounters may lead to shorter or fragmented tracking intervals, the present study focuses on a continuous visibility arc to isolate the intrinsic convergence properties of the distributed filter, rather than the scenario-dependent limitations of the observation geometry. Measurement noise is modeled as in (7) with standard deviation $\sigma_\theta = 10^{-4}$ rad. The measurement covariance is set as

$$\boldsymbol{\mathcal{R}} = \boldsymbol{I}_3 \, \sigma_\theta^2 \cdot 10^4,$$

while the process noise covariance is chosen as

$$\boldsymbol{Q} = \mathrm{diag}(10^{-7}, 10^{-7}, 10^{-7}, 10^{-9}, 10^{-9}, 10^{-9}),$$

properly scaled by the number of agents during the DEKF propagation step.

6. NUMERICAL RESULTS AND ANALYSIS

This section presents the results of the numerical simulations described in Sec. 5. The analysis compares the proposed Distributed Extended Kalman Filter (DEKF), a centralized EKF benchmark, and independent EKFs running on each agent without information exchange. Additional tests evaluate the impact of different initialization strategies for the DEKF covariance. Results are shown in terms of the estimation error evolution, reconstructed trajectories, and quantified using *Root Mean Square Error* (RMSE) statistics.

Qualitative Analysis of Estimation Errors

Figure 2 shows the orbital geometry of the observer constellation and the target. The three observers follow nearly identical orbital tracks, separated only by a small difference in mean anomaly, while the target orbit differs in inclination and semi–major axis, resulting in a natural drift. The initial positions of the observers are marked with dots, and both

the true and estimated target trajectories are shown. The DEKF estimate closely tracks the truth, and the zoomed view highlights the initial separation of the observers and the overlap of the estimated and true target orbits.

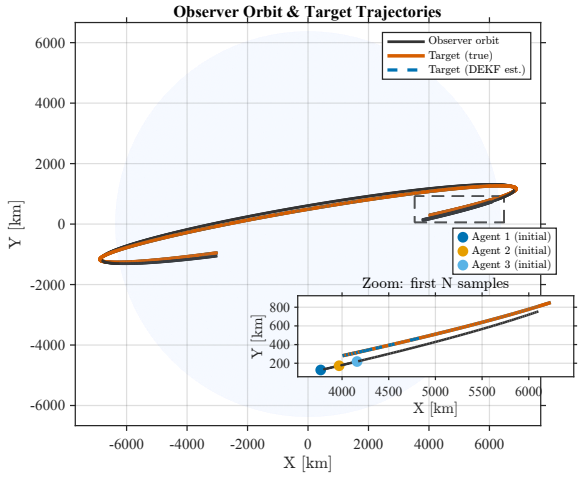

Figure 2. Observer constellation and target (true and estimated) orbit.

Figures 3 and 4 show the position and velocity error norms for the three considered approaches. The centralized EKF serves as a reference benchmark.

The DEKF exhibits performance that closely matches the centralized solution. The position error remains below 140 m during the first instants of the visibility window and decreases steadily to less than 5 m when the relative distance reaches 500 km and the target disappears from the observers' field of view. For velocity, the error peaks at approximately 3.6 m/s and converges to below 5×10^{-2} m/s at the end of the pass.

Independent EKFs, in contrast, show heterogeneous behaviors across agents. In this case, each filter only relies on its own angular measurements, leading to diverging estimates: position errors grow up to 650 m in the worst case and remain around 100 m at the end of the window. Velocity errors reach levels comparable to the DEKF at their maximum, but remain nearly twice as large at the end of the pass (about 10^{-1} m/s). These results prove that, without consensus, agents fail to converge toward a consistent target trajectory.

Impact of Covariance Initialization

An additional experiment investigates the role of the initial covariance $\mathbf{P}_0$ in the DEKF. Figure 5 compares the position errors obtained when $\mathbf{P}_0$ is computed via the covariance estimation procedure described in Sec. 3 against a manually tuned diagonal initialization. The tuned diagonal matrix was constructed by assigning equal values to the three position entries and a (different) equal value to the three velocity entries; these values were then refined through multiple trial runs until further adjustments produced negligible improvement. This manual tuning reflects common engineering practice but requires repeated offline trials and is sensitive to scenario parameters.

With the estimated covariance the maximum position error is about 140 m and rapidly decreases to $\sim$ 5 m by the end of the pass. In contrast, the tuned diagonal initialization

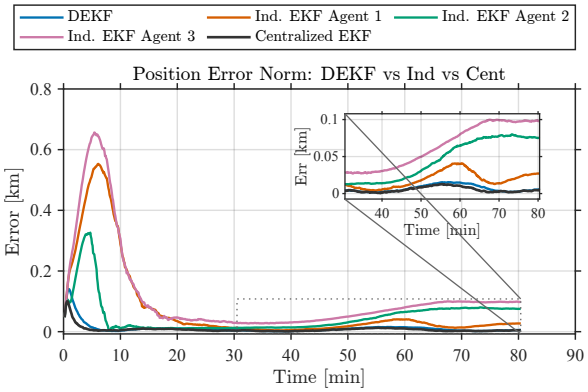

Figure 3. Position error norm: DEKF vs. centralized EKF vs. independent EKFs.

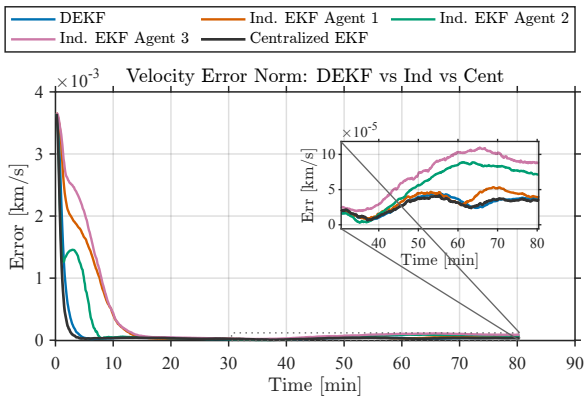

Figure 4. Velocity error norm: DEKF vs. centralized EKF vs. independent EKFs.

yields peaks up to $\sim$ 350 m, although both runs converge asymptotically to similar final accuracy for this particular scenario.

For velocity (Fig. 6), both initialization strategies lead to comparable peak and final errors, while the user-tuned covariance produces a larger mean error over the whole arc. These results highlight the benefit of a principled covariance initialization: it reduces the need for ad-hoc tuning and improves transient performance, which is critical in online operations where repeated trial-and-error is impractical.

Quantitative Analysis: RMSE Comparison

To provide a compact and insightful performance metric, we compute the Root Mean Square Error (RMSE) of position and velocity estimates with respect to the true target state. For a sequence of N estimation steps, the RMSE is defined as:

$$RMSE = \sqrt{\frac{1}{N}\sum_{k=1}^{N} ||\hat{x}_k - x_k||^2} \tag{46}$$

To better distinguish between transient behavior and asymptotic performance, the RMSE is computed over two distinct intervals: the *Full Window* (covering the entire pass) and the *Steady-State* (covering the last 60% of the simulation). The full-window metric captures the initialization quality and

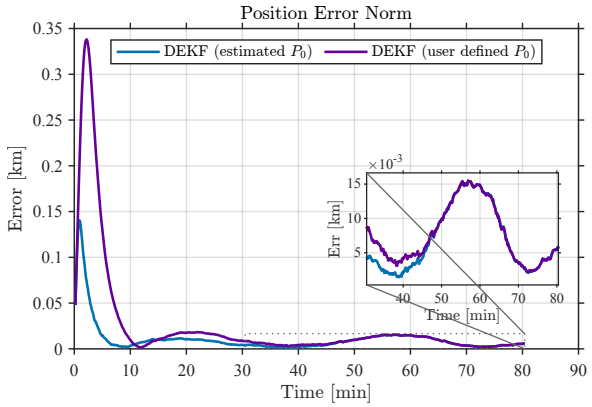

Figure 5. Position error norm: DEKF with estimated vs. user-defined covariance initialization.

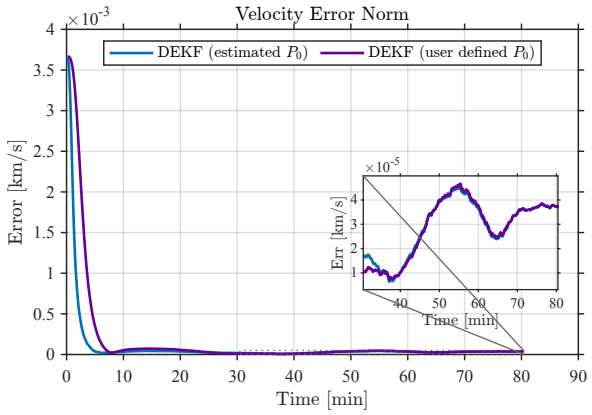

Figure 6. Velocity error norm: DEKF with estimated vs. user-defined covariance initialization.

convergence speed, while the steady-state metric reflects the ultimate accuracy limit imposed by sensor noise and geometry. Table 3 summarizes the RMSE values obtained through the simulations. The DEKF reduces errors by nearly one order of magnitude compared to independent filters, reaching steady-state errors of 8.5 m in position and 3×10^{-5} km/s in velocity, essentially matching the centralized performance benchmark.

Discussion

The numerical results highlight three main aspects:

1. The DEKF ensures accuracy that is comparable to the centralized EKF benchmark. Both position and velocity errors remain tightly bounded, with only marginal degradation compared to the centralized solution. This confirms that consensus-based information fusion is able to preserve the benefits of centralized estimation while operating in a distributed setting.
2. Independent EKFs, in contrast, produce heterogeneous estimates across agents. Since each filter relies solely on its own angular data, the resulting trajectories diverge and the estimation errors remain significantly larger even in the steady-state phase (up to 72 m position error vs 8.5 m for the DEKF). This underlines the importance of cooperation among observers: without information exchange, the network fails to build a consistent and accurate picture of the target state.
3. The choice of the initial covariance $\boldsymbol{P}_0$ plays a crucial role in the transient performance. Comparing the two DEKF initializations in Table 3, the steady-state RMSEs are nearly identical (8.5 m vs 8.7 m), confirming that both methods eventually converge to the same accuracy limit. However, the *Full Window* RMSE for the user-defined covariance is three times larger (64 m vs 21 m). This proves that the principled covariance estimation significantly improves robustness by minimizing the duration and magnitude of the initial transient error, without requiring the extensive manual tuning used for the benchmark.

Overall, the DEKF emerges as a scalable, robust, and communication-efficient alternative to centralized filtering. It enables each agent to reach a statistically consistent estimate by exchanging only compact information terms with its neighbors, preserving accuracy, reducing communication load, and ensuring robustness to network constraints.

7. Conclusions and Future Work

This paper has presented a complete framework for distributed angle-only relative orbit determination in satellite networks, combining a geometric initialization method, a novel analytical covariance derivation, and a distributed extended Kalman filter based on information consensus. The main strengths of the approach lie in its generality and consistency: the geometric initialization exploits only measurement geometry and remains dynamics-free, the closed-form covariance provides an analytically grounded quantification of uncertainty directly from sensor characteristics, and the distributed filter achieves estimation performance close to that of a centralized benchmark while avoiding the need for a fusion center. Numerical results in a realistic LEO scenario confirm that the proposed pipeline guarantees accurate and consistent estimates, with position errors of the order of tens and velocity errors below 10^{-4} km/s, demonstrating the effectiveness of cooperative angle-only navigation in mitigating the intrinsic observability limitations of single-observer geometries. The distributed filtering stage shows that consensus mechanisms can reproduce centralized accuracy while maintaining robustness to network topology constraints, and at the same time ensuring agreement among agents, unlike independent filters which diverge significantly. Beyond these quantitative results, the framework appears particularly promising for several reasons. It is inherently general and can be applied to different orbital regimes; it is purely angle-only, making it suitable for low-cost constellations of small satellites; it enables a complete end-to-end pipeline, from initialization to recursive estimation, without requiring any manual covariance tuning. Although the simulation scenario adopts some simplifications (synchronous measurements, perfectly known observer states), the achieved performance is very encouraging, especially considering that the ground truth was propagated with a high-fidelity SGP4 model, and leaves significant room for further exploration.

Future work will aim to progressively relax these simplifying assumptions and move toward the realization of a more realistic testbed. In particular, we plan to address asynchronous measurement availability, partial knowledge of observer states, and more complex communication topologies. Extending the approach to such scenarios will provide a clearer assessment of its practical applicability and robustness in real-world distributed satellite missions.

Table 3. RMSE of position and velocity estimates: Full Window vs. Steady-State (last 60%).

Filter	Pos. RMSE [km]		Vel. RMSE [km/s]	
	Full	Steady-State	Full	Steady-State
Ind. EKF Agent 1	0.1525	0.0220	6.5×10^{-4}	4.0×10^{-5}
Ind. EKF Agent 2	0.0773	0.0549	4.3×10^{-4}	6.0×10^{-5}
Ind. EKF Agent 3	0.1853	0.0721	7.2×10^{-4}	8.0×10^{-5}
DEKF (est. P_0)	**0.0207**	**0.0085**	$\mathbf{3.7 \times 10^{-4}}$	$\mathbf{3.0 \times 10^{-5}}$
DEKF (user P_0)	0.0635	0.0087	5.9×10^{-4}	3.0×10^{-5}
Centralized EKF	0.0130	0.0064	3.0×10^{-4}	3.0×10^{-5}

ACKNOWLEDGEMENTS

This work was partially supported by the Italian Ministry of Education and Research (MUR) within the framework of the FoReLab project (Departments of Excellence), by the Italian Space Agency (Agenzia Spaziale Italiana, ASI) under the research project "DORA - Determinazione Orbitale Relativa Autonoma on-board, con applicazioni terrestri e lunari," through agreement no. 2024-35-HH.0 (CUP n. F53C24000360001) between ASI and the University of Pisa.

REFERENCES

[1] S. Kazemi, N. L. Azad, K. A. Scott, H. B. Oqab, and G. B. Dietrich, "Orbit determination for space situational awareness: A survey," *Acta Astronautica*, 2024.

[2] H. Yunpeng, L. Kebo, L. Yan'gang, and C. Lei, "Review on strategies of space-based optical space situational awareness," *Journal of Systems Engineering and Electronics*, vol. 32, no. 5, pp. 1152–1166, 2021.

[3] C. Dai, H. Qiang, D. Zhang, S. Hu, and B. Gong, "Relative orbit determination algorithm of space targets with passive observation," *Journal of Systems Engineering and Electronics*, vol. 35, no. 3, pp. 793–804, 2024.

[4] S. Palo, G. Stafford, and A. Hoskins, "An agile multiuse nano star camera for constellation applications," 2013.

[5] D. C. Woffinden and D. K. Geller, "Observability criteria for angles-only navigation," *IEEE Transactions on Aerospace and Electronic Systems*, vol. 45, no. 3, pp. 1194–1208, 2009.

[6] I. Klein and D. K. Geller, "Zero δv solution to the angles-only range observability problem during orbital proximity operations," in *Itzhack Y. Bar-Itzhack Memorial Symposium on Estimation, Navigation, and Spacecraft Control*. Springer, 2012, pp. 351–369.

[7] G. Gaias, S. D'Amico, and J.-S. Ardaens, "Angles-only navigation to a noncooperative satellite using relative orbital elements," *Journal of Guidance, Control, and Dynamics*, vol. 37, no. 2, pp. 439–451, 2014.

[8] D. K. Geller and T. A. Lovell, "Angles-only initial relative orbit determination performance analysis using cylindrical coordinates," *The Journal of the Astronautical Sciences*, vol. 64, no. 1, pp. 72–96, 2017.

[9] A. Perez, D. Geller, and T. Lovell, "Non-iterative angles-only initial relative orbit determination with j2 perturbations," *Acta Astronautica*, vol. 151, pp. 146–159, 2018.

[10] T. A. Lovell, A. J. Sinclair, and B. Newman, "Angles only initial orbit determination: Comparison of relative dynamics and inertial dynamics approaches with error analysis," in *2018 Space Flight Mechanics Meeting*, 2018, p. 0475.

[11] S. D'Amico, J.-S. Ardaens, G. Gaias, H. Benninghoff, B. Schlepp, and J. Jørgensen, "Noncooperative rendezvous using angles-only optical navigation: system design and flight results," *Journal of Guidance, Control, and Dynamics*, vol. 36, no. 6, pp. 1576–1595, 2013.

[12] G. Gaias and J.-S. Ardaens, "In-orbit experience and lessons learned from the avanti experiment," *Acta Astronautica*, vol. 153, pp. 383–393, 2018.

[13] B. D. Tapley, S. Bettadpur, M. Watkins, and C. Reigber, "The gravity recovery and climate experiment: Mission overview and early results," *Geophysical research letters*, vol. 31, no. 9, 2004.

[14] G. Krieger, A. Moreira, H. Fiedler, I. Hajnsek, M. Werner, M. Younis, and M. Zink, "Tandem-x: A satellite formation for high-resolution sar interferometry," *IEEE transactions on geoscience and remote sensing*, vol. 45, no. 11, pp. 3317–3341, 2007.

[15] J. Burch, T. Moore, R. Torbert, and B.-h. Giles, "Magnetospheric multiscale overview and science objectives," *Space Science Reviews*, vol. 199, no. 1, pp. 5–21, 2016.

[16] S. D'Amico, "Autonomous nanosatellite swarming using radio-frequency and optical navigation (ans)," *NASA Fact Sheet, Stanford Space Rendezvous Lab (SLAB)*, 2018.

[17] Y. Hu, I. Sharf, and L. Chen, "Three-spacecraft autonomous orbit determination and observability analysis with inertial angles-only measurements," *Acta Astronautica*, vol. 170, pp. 106–121, 2020.

[18] "Distributed orbit determination and observability analysis for satellite constellations with angles-only measurements."

[19] B. Jia, K. D. Pham, E. Blasch, D. Shen, Z. Wang, and G. Chen, "Cooperative space object tracking using space-based optical sensors via consensus-based filters," *IEEE Transactions on Aerospace and Electronic Systems*, vol. 52, no. 4, pp. 1908–1936, 2016.

[20] J. Kruger, K. Wallace, A. W. Koenig, and S. D'Amico, "Autonomous angles-only navigation for spacecraft swarms around planetary bodies," in *2021 IEEE Aerospace Conference (50100)*. IEEE, 2021, pp. 1–20.

[21] J. Hippelheuser and T. Elgohary, "A novel approach for initial orbit determination for space-based observation networks," in *Proceedings of the 3rd IAA Conference on Space Situational Awareness, Madrid, Spain*, 2022.

[22] H. Long, Z. Qu, X. Fan, and S. Liu, "Distributed extended kalman filter based on consensus filter for

wireless sensor network," in *Proceedings of the 10th World Congress on Intelligent Control and Automation*. IEEE, 2012, pp. 4315–4319.

[23] F. R. Hoots and R. L. Roehrich, "Models for propagation of norad element sets," 1980.

[24] M. Mahooti, "Sgp4," https://www.mathworks.com/matlabcentral/fileexchange/62013-sgp4, accessed: August 2025.

BIOGRAPHY

Giovanni Romagnoli is a PhD candidate in Information Engineering at the University of Pisa. He holds a master's degree in Robotics and Automation Engineering. His doctoral fellowship, funded by the Italian Space Agency (ASI), focuses on on-board relative orbit determination for spacecraft. This innovative approach enables the accurate tracking and orbit estimation of space objects directly on-board the spacecraft. Giovanni also contributes to the ASI MUSAPOEM project, which focuses on Multi-Satellite Proximity Operations. His work, which develops relative navigation algorithms for spacecraft proximity operations directly complements his doctoral research, with the shared goal of enhancing the autonomy and safety of space missions.

Giordana Bucchioni is a researcher at the Department of Information Engineering, University of Pisa, working in the scientific-disciplinary area of control and robotics (Automatica, IINF-04/A). She holds a PhD from Pisa and her doctoral thesis, focused on guidance and control in three-body lunar space missions, was awarded the "Guido Horn d'Arturo" prize by the Italian Astronomical Society . Her research interests include spacecraft dynamics, rendezvous docking, and GNC (guidance, navigation, and control) in cislunar trajectories . She has collaborated with national and international institutions such as the Italian Space Agency (ASI), ESA, and ISAE-SUPAERO. In recognition of her scientific contributions and role as a woman in engineering, she was awarded the "She Made a Difference" prize by EWMD La Spezia .

Giusy Falcone received the B.S. and M.S. degrees in Aerospace Engineering from the University of Pisa, Italy, in 2014 and 2017, respectively, and the Ph.D. degree in Aerospace Engineering from the University of Illinois at Urbana-Champaign in 2022. She is currently an Assistant Professor in the Department of Aerospace Engineering at the University of Michigan and serves as the Principal Investigator of the Space-Flight Autonomous Leading CONcepts (Space-FALCON) Lab. Her research focuses on guidance, control, and autonomous decision-making for hypersonic and space vehicles.